Spectral and thermometric properties altering through crystal field strength modification and host material composition in luminescent thermometers based on Fe^{3+} doped AB_2O_4 type nanocrystals (A= Mg, Ca; B=Al, Ga)

K.Kniec[1*], W. Piotrowski[1], K. Ledwa[1], L. D. Carlos[2], L. Marciniak[1*]

[1]Institute of Low Temperature and Structure Research, Polish Academy of Sciences, Okólna 2, 50-422 Wroclaw, Poland

[2] Phantom-g, CICECO-Aveiro Institute of Materials, Department of Physics, University of Aveiro, Campus de Santiago, 3810-193 Aveiro, Portugal

*** corresponding author: *k.kniec@intibs.pl*, *l.marciniak@intibs.pl***

KEYWORDS: iron, terbium, luminescence, crystal field, spinel, luminescent nanothermometry

Abstract

The growing interest in the use of luminescence thermometry for noncontact temperature reading in very specific conditions imposes the need to develop an approach allowing modification of the luminescence parameters of the thermometer accordingly to the requirements. Therefore, in response to these expectations, this manuscript reports an approach to modulating the spectral position and the luminescence thermal quenching rate of Fe^{3+} ions by modifying the crystal field strength and the host material composition of nanocrystalline AB_2O_4 type nanocrystals (A= Mg, Ca; B=Al, Ga). It was proved that in a group of $MgAl_2O_4$, $MgGa_2O_4$, $CaAl_2O_4$, and $CaGa_2O_4$ nanocrystals doped with Fe^{3+} ions the emission spectral range, as well as the relative thermal sensitivity (from 0.2%/ºC for MAO to 2.07%/ºC for CGO) and the operating temperature range, can be easily modified by the host material composition. For instance, a maximal relative thermal sensitivity of 2.58%/ºC is obtained for Fe^{3+}, Tb^{3+} co-doped $CaAl_2O_4$ nanocrystals. The proposed approach is a step toward the intentional designing of the highly sensitive luminescent thermometer.

Introduction

Spinel type compounds of the general formula AB_2O_4, are widely investigated as host materials for transition metal (TM) ions dopants, because in their crystallographic structure both octahedrally (A) and tetrahedrally (B) coordinated cationic sites can be found, which are especially desired to obtain bright TM luminescence. Additionally, spinels are well known from their high chemical and thermal stability and high resistance to the radiation damage[1–6]. Presented features make these compounds attractive phosphors for the manifold type of applications including light-emitting diodes (LED), liquid crystal devices (LCD) backlights, persistent luminescence and bioimaging [7–9]. Due to the high susceptibility of their emission intensity to thermal quenching, TM ions are very attractive optically active centers for noncontact temperature sensing[10–12]. Therefore, spinels are host materials of great importance for this type of applications[13–16]. An additional advantage of TM-doped luminescent thermometers is the easiness in the tunability of their optical properties including the spectral range of optical response, emission brightness and the luminescence thermal quenching rate, through the crystal field engineering. Therefore, the family of spinels due to the great number of its representatives, and thus, a wide possibility of host material modification is very appealing for luminescent thermometry. However, the number of studies on spinel doped TM nanocrystals for luminescent thermometry is strongly limited. The majority of the research concerning nanocrystalline TM doped spinels is devoted to their persistent luminescence and its application in tumor targeting and detection [17–23]. To the best of our knowledge, only a few literature reports are describing the utilization of TM doped spinels for luminescent thermometry[24–28] Kobylinska *et al.* investigated the influence of dopant concentration on the thermometric properties of $MgAl_2O_4$:Co^{2+}, Nd^{3+} nanocrystals revealing that the highest relative thermal sensitivity, S_R=0.28%/^{o}C, was obtained for 0.01% Co^{2+} and 5% Nd^{3+} [24]. Significantly higher value, S_R=2.8%/^{o}C at 310 ^{o}C, was reported by Ueda et al. for the $ZnGa_2O_4$:Cr^{3+} polycrystalline ceramic, where the luminescence thermal response is based on the $^4T_2 \rightarrow {}^4A_2$ to $^2E \rightarrow {}^4A_2$ emission intensity ratio [25]. An interesting approach was reported by Glais *et al.*, who take advantage of the thermally induced temporal changes of persistent luminescence of $ZnGa_2O_4$:Cr^{3+},Bi^{3+}

nanocrystals. These studies developed a luminescent nanocrystalline thermometer with S_R=1.7%/ºC at 190ºC [26]. Even higher relative sensitivity was reported by Yang *et al* who created a luminescent thermometer based on the persistent luminescence of $ZnGa_{2-x}Ge_xO_4:Cr^{3+}$ reaching 4.7%/ºC at 54ºC [27]. The lifetime based luminescent thermometers based on $ZnGa_2O_4:Cr^{3+}$ glass-ceramics with S_R=0.6%/ºC at 149ºC were reported by Chen *et al* [28]. As presented above the main limitation of ratiometric luminescent thermometers based on TM-doped spinels, especially those emitting in the near-infrared (NIR) spectral range is their low relative thermal sensitivity. Different approaches to enhance the S_R values of TM-based luminescent nanothermometers have been proposed, including the optimization of the concentration of the dopant, grain size, and activation of additional channels of nonradiative depopulation of the emitting states (such as phonon-assisted energy transfer by introducing wisely selected co-dopants[24,29–33]). However, one of the most promising and spectacular effects concerning the improvement of thermal susceptibility of TM luminescence can be achieved by the modification of the activation energy of the thermal quenching process via the modulation of the relative position of excited and ground state parabolas. This can be reached by varying the cationic composition in inorganic lattices and thereby the modification of crystal field strength (CFS). This vulnerability results from the fact, that the valence electrons in *3d* orbital are directly exposed to the environmental changes, including crystallographic surroundings. This approach has been successfully implemented in the case of Cr^{3+} , Fe^{3+}, Ni^{2+} and Mn^{3+}/Mn^{4+}- based luminescent thermometers (LTs) [29,34–36], where the elongation of metal-oxide (M-O) distance (R, CFS~R^{-5}) increases the probability of nonradiative depopulation of the excited parabola and hence facilitating the luminescence thermal quenching. Since the A and B sites in spinel structure are substituted by optically active ions, the modification of their composition may significantly improve the tunability of spinel-based phosphors and thus may lead to the expansion of their application area[37]. As it has been recently proved that Fe^{3+} ions can be successfully used as an optically active dopant for bright red luminescence of high susceptibility to thermal quenching which indicates their high potential for temperature sensing[29,38]. However, up to date no systematic studies concerning the influence of host material composition on the thermometric performance

of Fe^{3+} nanocrystalline spinels have been reported. The main idea which stands behind the approach presented in this manuscript is shown in Figure 1. In the case of Fe^{3+} ions, according to the Tanabe-Sugano diagram for the high spin (HS) d^5 configuration, the increase of the crystal field strength should cause the redshift of the emission band and the enhancement of the luminescence thermal quenching. Thus, by increasing the M-O distance (modified by the composition of the host material) phosphors with a broad emission band localized in the near infrared spectral range and with high sensitivity to thermal changes will be obtained. However, when cations of bigger ionic radii are incorporated into the host material, and only the tetragonal sites are possible to be occupied by the Fe^{3+} ions, the spectroscopic properties of Fe^{3+} ions will change drastically. A much broader emission band with the maxima shifted toward longer wavelenths and an increase in the thermal quenching are expected in this case. Therefore, the aim of this paper is to investigate how the composition of the spinel and the local ion's environment affects the spectroscopic properties of the Fe^{3+} ions and thus the thermometric properties of Fe^{3+}-based luminescent thermometer. For this purpose, four spinels of different cations in the A and B sites were selected and their optical properties have been systematically investigated i. e. $MgAl_2O_4$, $MgGa_2O_4$, $CaAl_2O_4$, $CaGa_2O_4$. The influence of the crystal field strength and host material composition on the spectral position of the emission band and thermal stability of the Fe^{3+} luminescence was investigated in order to develop a highly sensitive nanocrystalline luminescent thermometer operating in intensity, ratiometric mode. In order to obtain high relative thermal sensitivity and reliability of temperature readout the emission of Tb^{3+} co-dopant ions was chosen as an internal reference[39,40]. The Tb^{3+} ions are well known from their intense green emission associated with the $^5D_4 \rightarrow {}^7F_5$ electronic transitions, which is spectrally well separated from the Fe^{3+} emission band. Moreover, the energy difference between the $^5D_4$ and $^7F_0$ energy levels (around 15 000cm^{-1}) sufficiently prevents the $^5D_4$ thermal quenching by the multiphonon nonradiative depopulation.

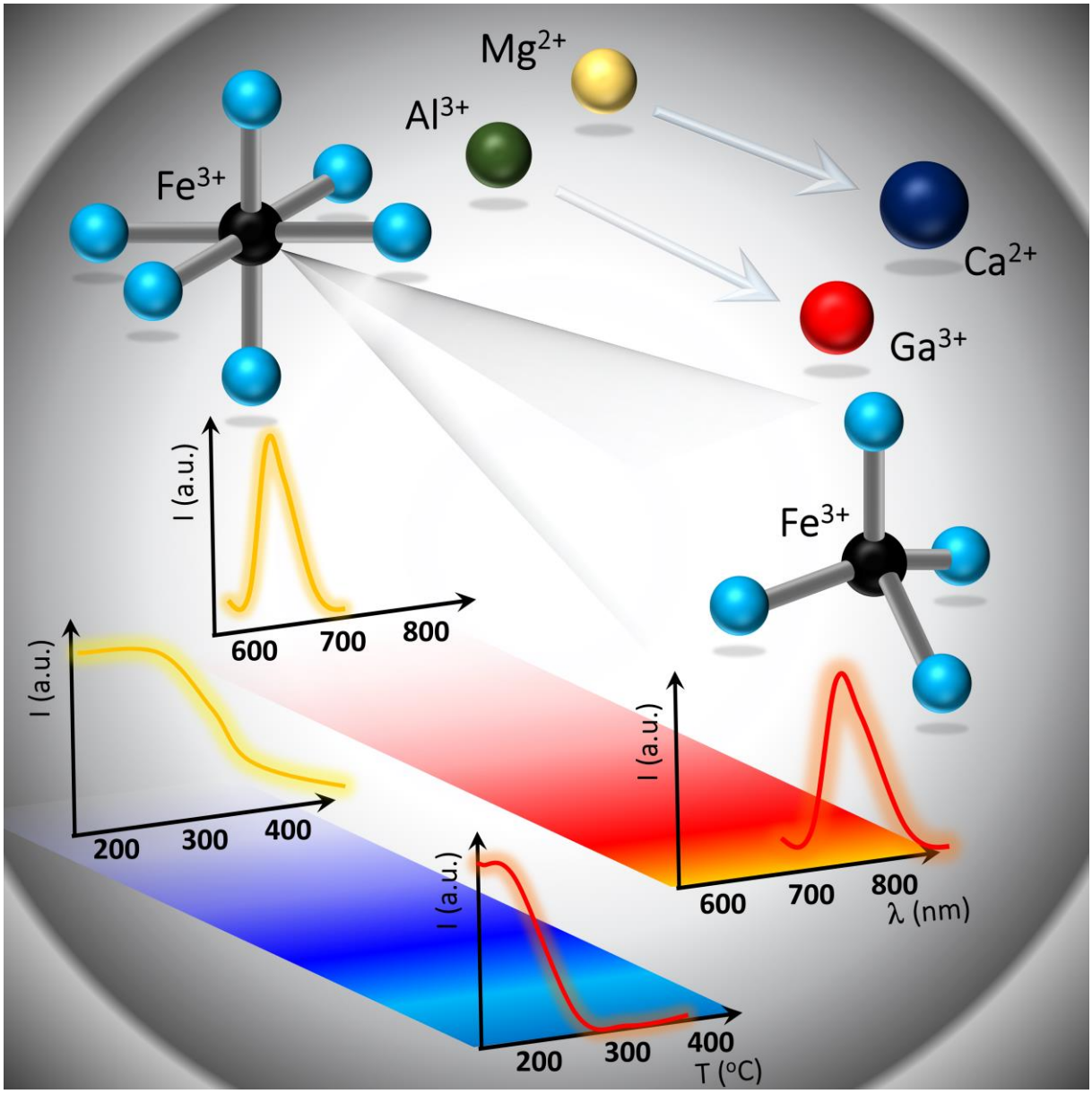

Fig. 1. The visualization of the concept of the modification of the spectral and thermal properties of the Fe^{3+}-doped spinels by the crystal field strength modulation and host material composition.

Experimental

Synthesis of Fe^{3+}-doped nanocrystals

The investigated nanocrystalline materials with the chemical formula of $MgAl_2O_4$ (MAO), $MgGa_2O_4$ (MGO), $CaAl_2O_4$ (CAO), $CaGa_2O_4$ (CGO) doped with Fe^{3+} ions have been synthesized by the modified

Pechini method. In order to minimize the probability of luminescence concentration quenching the Fe^{3+} concentration was set to be 0.1% with respect to Al^{3+} or Ga^{3+} ions. Magnesium nitrate hexahydrate ($Mg(NO_3)_2 \cdot 6H_2O$ of 99.999% purity from Alfa Aesar), calcium nitrate tetrahydrate ($Ca(NO_3)_2 \cdot 4H_2O$ of 99.999% purity from Alfa Aesar), aluminum nitrate nonahydrate ($Al(NO_3)_3 \cdot 9H_2O$ of 99.999% purity from Alfa Aesar), gallium nitrate nonahydrate ($Ga(NO_3)_3 \cdot 9H_2O$ of 99.999% purity from Alfa Aesar) and iron nitrate nonahydrate ($Fe(NO_3)_3 \cdot 9H_2O$ of 99.999% purity from Alfa Aesar), citric acid (CA, $C_6H_8O_7$ of 99.5+% purity from Alfa Aesar) and polyethylene glycol (PEG-200, from Alfa Aesar) were used as starting compounds. Stoichiometric quantities of appropriate nitrates were dissolved in distilled water and magnetically stirred with CA for 2 h at 90°C on the heating stage. The CA, acting as a complexing agent, was used in the double excess in respect to the total molar amount of all metal ions (Mg^{2+}/Ca^{2+}/, Al^{3+}/Ga^{3+} and Fe^{3+}). Afterwards, an adequate volume of PEG-200 was added dropwise to the aqueous solution of metal complexes, which was subsequently magnetic stirred at 90°C for 1 h. This step led to the polyesterification process between CA and PEG which was aimed at the providing of separation of emerging nanocrystals. Then, the reaction mixture was dried at 90°C for one week. After this time the created polymeric resin was annealed in the air for 8 h at 850°C in order to obtain the powder form of the nanomaterials.

Synthesis of Fe^{3+}, Tb^{3+} -co-doped nanocrystals

MAO, MGO, CAO and CGO nanocrystals co-doped with Fe^{3+} and Tb^{3+} ions were synthesized in the same way as the singly Fe^{3+} doped counterparts described above. The additional step was related to the obtaining of terbium nitrate ($Tb(NO_3)_3$) through the recrystallization process. To this aim, stoichiometric amounts of terbium oxide (Tb_4O_7 with 99.999% purity from Stanford Materials Corporation) were dissolved in distilled water and ultrapure nitric acid (65%). The formed nitrate was recrystallized three times using a small volume of distilled water. After this synthesis, the received solutions were dried for 1week at 90◦C. Finely

the deliberate products were obtained by annealing in the air for 8 h at 850◦C. The concentration of Fe^{3+} was 0.1% and the concentration of Tb^{3+} was 1% in respect to the Mg^{2+} and Ca^{2+} ions.

Characterization

Powder diffraction studies were carried out on PANalytical X'Pert Pro diffractometer equipped with Anton Paar TCU 1000 N Temperature Control Unit using Ni-filtered Cu *Kα* radiation (V = 40 kV, I = 30 mA). The Raman spectra were recorded at room temperature using an InVia confocal microscope from Renishaw supplied with a silicon CCD camera as a detector, employing the 488 nm excitation line and under a 20× objective with spatial resolution lower than 1 μm. Transmission electron microscope images were obtained using a TEM Philips CM-20 SuperTwin operating at 160 kV with an optical resolution of 0.25 nm. The emission spectra were measured using the 266 nm excitation line from a laser diode (LD) and a Silver-Nova Super Range TEC Spectrometer form Stellarnet (1 nm spectral resolution) as a detector. The temperature of the sample was controlled using a heating stage from Linkam (0.1 ^{o}C temperature stability and 0.1 ^{o}C set point resolution). Excitation spectra were measured using FLS1000 Fluorescence Spectrometer form Edinburgh Instruments. Luminescence decay profiles were recorded using FLS1000 Fluorescence Spectrometer from Edinburgh Instruments with μFlash lamp as an excitation source and R928P side window photomultiplier tube from Hamamatsu as a detector. Temperature-dependent luminescent lifetime was controlled using the abovementioned heating stage from Linkam.

Results and discussion

The XRD technique was used to verify the phase purity of the synthesized Fe^{3+}-doped nanocrystals. As it can be observed, the diffraction Bragg reflectionsof all of the obtained phosphors correspond to the reference patterns, which confirms their well-crystallized structures (Fig. 2a). The comparison of the structural parameters of the obtained host materials is presented in Table 1[24]. The lack of additional Bragg reflections in the representative experimental patterns confirmed that Fe^{3+} well substitutes cationic sites in spinels. The structure of the magnesium aluminum spinel consists of six-fold and four-fold coordinated

sites of Al^{3+} and Mg^{2+}, respectively, where the Fe^{3+} ions substitute the octahedral ones $(AlO_6)^{9-}$ [24] (Fig. 2 b). In the case of $MgGa_2O_4$ both Ga^{3+} and Mg^{2+} ions are surrounded by four and six O^{2-} ligands. Correspondingly, the percentage site occupation of octahedra for Ga^{3+} and Mg^{2+} ions are 59% and 82%, respectively[41], where the Fe^{3+} ions preferentially replace the Ga^{3+} ions in the $(GaO_6)^{9-}$ crystallographic position due to the difference in the ionic radii between substituted and dopant ions Al^{3+}_{octa} (0.68 Å), Ga^{3+}_{octa} (0.76 Å) and Fe^{3+}_{octa} (0.69 Å) (Fig. 2 c)[29].Weidenborner et al reported that in the case of the MGa_2O_4 crystals below 1200 K an inverted spinel structure was obtained[]. In the case of the inverted spinels, both the octahedral and tetrahedral sites of Ga^{3+} can be occupied by the Fe^{3+} ions. Some of the previously published reports reveal that even in the case of the $MgAl_2O_4$ the cation disorder may lead to the occurrence of $(AlO_4)^{5-}$ tetrahedrals. This great number of possible sites to be occupied by the Fe^{3+} ions increases the complexity of the problem and additional analysis of the spectroscopic properties of the Fe^{3+} ions is needed. In the case of $CaAl_2O_4$, which consists of tetrahedral Al^{3+} ions sites and Ca^{2+} sites with the coordination numbers of six $(CaO_6)^{10-}$ and nine $(CaO_9)^{16-}$, Fe^{3+} ions preferentially occupy the $(AlO_4)^{5-}$ sites [42–44] (Fig. 2 d). The Ga^{3+} substitution by Fe^{3+} dopant is also favoured in the case of $CaGa_2O_4$ nanocrystals, which is formed by Ga^{3+} ions in tetrahedral coordination and two crystallographically inequivalent Ca^{2+} sites, i. e. surrounded by seven O^{2-} ions and eight O^{2-} (Fig. 2 e).. It needs to be noted here that $CaGa_2O_4$ materials may crystallize in both orthorhombic and monoclinic structures,[45,46] however, the XRD studies confirmed the orthorhombic structure of obtained phosphor (Figure 2a) . The differences in the site occupation in the considered group of materials lead to the enlargement of the cell parameter *a* in the case of CAO and CGO, whereas to the reduction for MAO and MGO ones (Fig. S1 a). The average grain size, calculated using the Rietveld refinement of the diffraction patterns, increases in the following order: MAO (10.3 nm), MGO (12.5 nm), CAO (24.9 nm) and CGO (58.5 nm) which correspond with the enhancement of *a* cell parameter, namely $a_{MAO} < a_{MGO} < a_{CAO} < a_{CGO}$ (Fig. S1 a). The smallest size of magnesium-based spinels, is associated with the smaller ionic size of Mg^{2+} in respect to Ca^{2+} ions (Fig. 2 a). Another reason for this phenomenon could be explained based on thermodynamics. The enthalpy for cubic crystal system (MAO and MGO) are

higher than for structures of lower symmetry (CAO and CGO). It is tantamount to much more energy which is required to the crystallization of $MgAl_2O_4$ and $MgGa_2O_4$ materials. The analysis of the morphology of obtained nanocrystals using TEM technique indicates that the investigated materials consist of crystallized and aggregated crystals, whereas the smallest grain size was found for $MgAl_2O_4$ and $MgGa_2O_4$ phosphor, staying in agreement with obtained XRD patterns (Fig. 2 f-i). The aggregation of the nanocrystals can be the reason of the last synthesis step, namely the annealing process at 850°C for 8 h. Because the luminescent properties of the phosphors are strongly dependent on the phonon energy of the host material, the Raman spectra (Fig. S 1b) were measured indicating that the peaks in the spectrum of $MgAl_2O_4:Fe^{3+}$ between 250 and 550 cm^{-1} are related to the rotational modes of the same group, where the other peaks with energies higher than 550 cm^{-1} may be assigned to the stretching vibrations of $(AlO_6)^{9-}$ octahedra. For $CaAl_2O_4:Fe^{3+}$ nanomaterials the intense peak at 520 cm^{-1} is attributed to the vibrations of bridging oxygen atoms within the Al–O–Al linkages. The position of Raman peaks in the spectrum of the $MgGa_2O_4:Fe^{3+}$ phosphor with the maximum at 634 and 750 cm^{-1} correspond to the antisymmetric and symmetric stretching of $(GaO_6)^{9-}$, respectively. In the case of $CaGa_2O_4:Fe^{3+}$ nanocrystals the dominant peaks at 541 cm^{-1} and 590 cm^{-1} in the Raman spectrum, which are associated with the Ga-O-Ga bridges between $(GaO_4)^{5-}$ tetrahedra. The peaks with higher energies (620 cm^{-1}, 660 cm^{-1}) are characterized for stretching vibrations of $(GaO_4)^{5-}$ tetrahedra. The Tb^{3+} ions (r= 1.18 Å) occupy the crystallographic environment of Mg^{2+} and Ca^{2+} ions consisting of four, six, nine and eight O^{2-} ions in the structure of MAO (r_{Mg}=0.71 Å), MGO (r_{Mg}=0.86 Å), CAO (r_{Ca}= 1.18 Å), and CGO (r_{Ca}= 1.12 Å), respectively[5,47–49]. The simultaneous presence of Fe^{3+} and Tb^{3+} ions in the spinel host materials does not cause separation of any additional crystallographic phase (Fig. S1 c).

Table 1. Structural parameters of spinel host materials

Parameter	**MAO**	**MGO**	**CAO**	**CGO**
ICSD code	290114	82915	260	21042
Crystal system	cubic	cubic	monoclinic	orthorhombic

Space group	*Fd-3mZ (227)*	*Fd-3mZ (227)*	*P21/n (11)*	*Pna2$_1$ (33)*
a cell parameter [Å]	8.0850	8.2880	8.7000 8.75189 Å	10.1890
Al^{3+}/Ga^{3+} - O^{2-} distance	1.9292	2.0172	1.7540	1.8146
Mg^{2+}/Ca^{2+} - O^{2-} distance	1.9186	2.0172	2.42143	2.541529

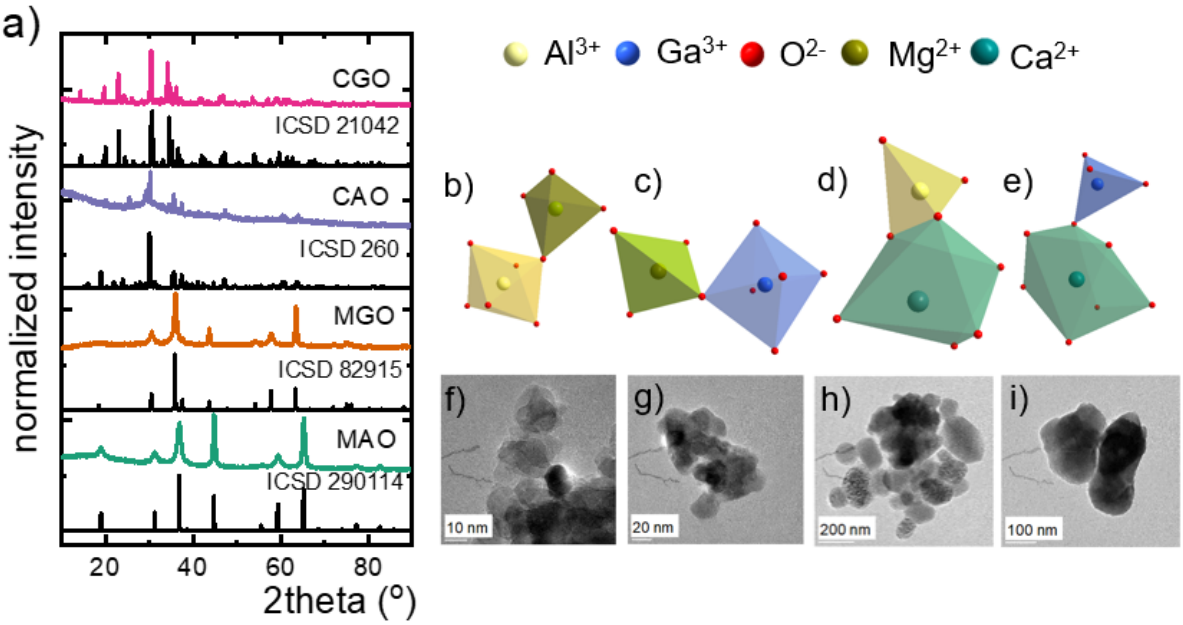

Fig. 2. XRD patterns of spinels nanocrystals doped with Fe^{3+} ions –a); the visualizations of the cationic polyhedral of MAO–b),, MGO- c), CAO - d) and CGO structures - e), and the corresponding representative TEM images of Fe^{3+} doped MAO –f), MGO –g), CAO –h), CGO –i).

To understand the luminescent properties of Fe^{3+} doped nanocrystals the configurational coordinate diagram of Fe^{3+} ions is presented in Fig. 3a. In our experiment, the ultraviolet (UV) excitation of λ_{exc}=266 nm, which leads to the occurrence of the $O^{2-}\rightarrow Fe^{3+}$ charge-transfer transition, was used. The nonradiative depopulation of the ground state of Fe^{2+} ions leads to the increase in the population of $^4T_1$ (^4G) state, followed by its radiative depopulation to the ground $^{26}A_1$ (^6S) state. The $^4T_1$ (^4G)$\rightarrow$$^6A_1$ (^6S) electronic transition leads to the appearance of the broad emission band in the red/NIR spectral range (Fig. 3 a, b). It was found that the energy of the spectral position of the emission band is strongly dependent on the host material composition and undergoes redshift with the elongation of the metal-to-oxygen distance (R) from 696 nm (MGO) to 809 nm (CGO) (Fig. 3 b). This effect may be explained in terms of the lowering of the crystal field strength (CFS) which is reciprocally proportional to the R as follows: CFS~R^{-5}. Therefore the

increase of CFS leads to the lowering of the energy of emission bands maximum as shown in Fig. 3c. The relatively small value of the spectral bandwidth observed for MGO and MAO confirms that the Fe^{3+} ions occupy the octahedral sites. However, the spectral bandwidth of the CAO:Fe^{3+} and CGO:Fe^{3+} is significantly broader with respect to the those of MAO:Fe^{3+} and MGO Fe^{3+}. This effect is in agreement with the expectation for Fe^{3+} ions in tetrahedral coordination. However, in the case of the HS d^5 electronic configuration the change of the coordination from octahedral to the tetrahedral causes the blueshift of the emission band as shown by Kovalenko et al for Mn^{2+} ions. Therefore, the obtained results may be explained in terms of the distortion of the Al^{3+}/Ga^{3+} polyhedra which lowers the symmetry of the local ion to C_1. This symmetry reduction will split the triply orbitally degenerate $^4T_1$ state into three non-degenerated ^4A states. Such a modification of the point symmetry must enhance the probability of radiative transitions and hence a shorter lifetime of the Fe^{3+} excited state is expected. This is in agreement with the results presented in Fig. 3d.

In the excitation spectra recorded at -150°C for $^4T_1$ (^4G)→$^2T_2$ emission the broad band with the maximum at 277 nm which is attributed to the O^{2-}→Fe^{3+} charge transfer transition dominates (Fig. S2). Additionally, three absorption bands related to the *d-d* electronic transition are observed, coming from Fe^{3+} centers. The bands in the 320 – 350 nm and 440 – 480 nm spectral ranges are assigned to the $^6A_1$ (^6S) → $^4T_2$ (^4D) and $^6A_1$ (^6S) → $^4A_1$, ^4E (^4G), respectively[50]. However, the $^6A_1$ (^6S) → $^4T_2$ (^4D) transition was not observed in the case of CGO material. It is evident, that the $^6A_1$ (^6S) → $^4A_1$, ^4E (^4G) excitation band is red-shifted along with the change of the host material composition from MGO to CGO and the increase of its splitting can be observed, what clearly confirms the reduction of the local symmetry from T_d to C_1. Besides, the spectral position of intense excitation belonging to the $^6A_{1g}$ (^6S) → ^4E_g (^4D) transition undergoes the displacement towards longer wavelengths in the same order which was found for the emission spectrum, namely MGO, MAO, CAO and CGO (Fig. 3 b, c, Fig. S2).

It is well known that the CFS affects not only the spectral position of the emission band but also the decay profile of the TM luminescence. The low temperature luminesce lifetime of $^4T_1$ excited state is strongly

influenced by host material composition and its value undergoes monotonical shortening along with the decrease of CFS, namely τ=8.38 ms for MAO, τ=7.66 ms for MGO, τ=3.27 ms for CAO and τ=0.27 ms for CGO nanocrystals (Fig. 3 d, Fig. S3). This phenomenon can be explained in terms of the change of the ions local symmetry and an increase of the nonradiative relaxation of the excited state which increases due to the shortening of the energy gap between the ground and excited states and with the change of the activation energy discussed later in the manuscript.

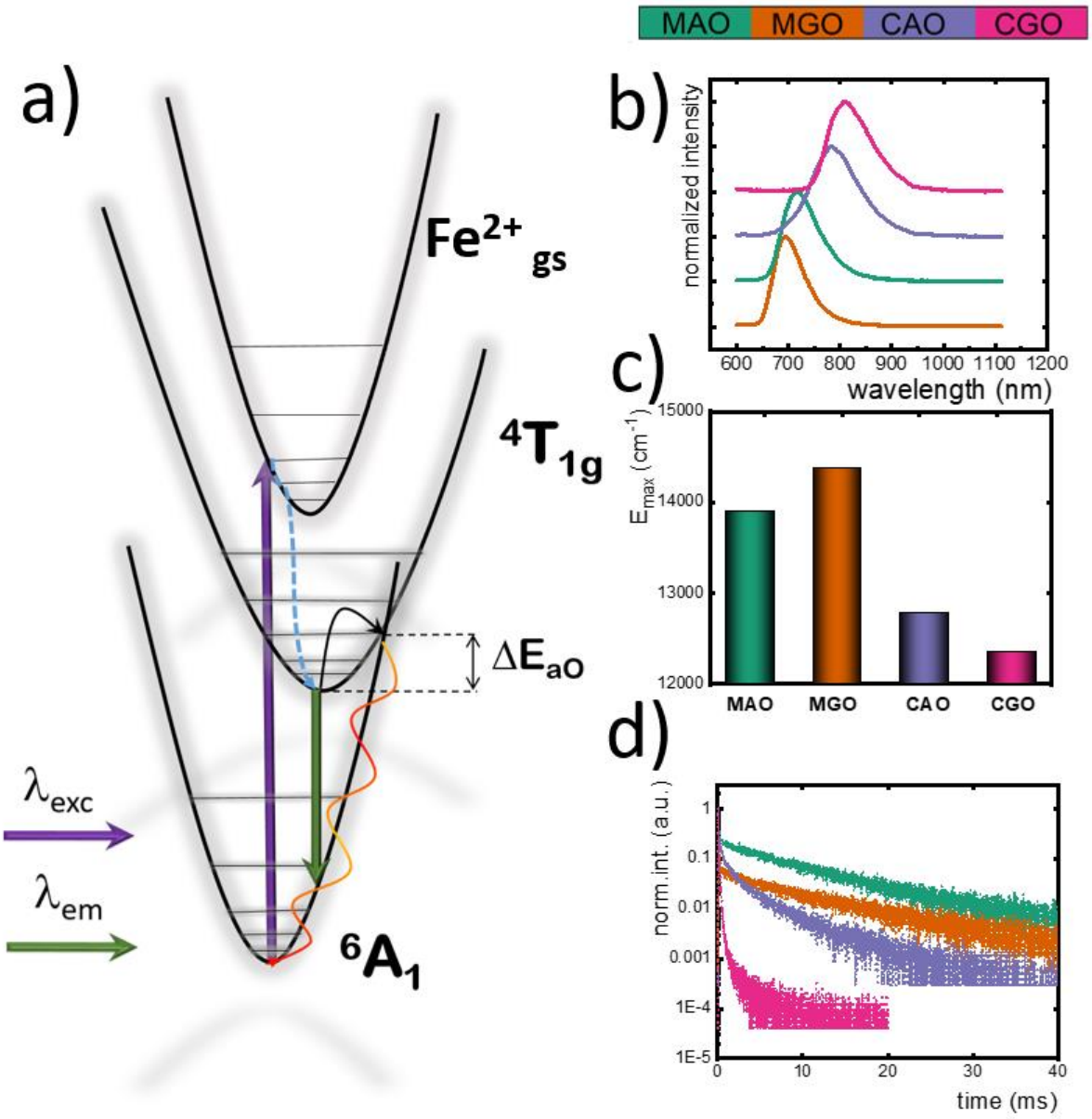

Fig. 3. The schematic configurational coordination diagrams of Fe^{3+} ions in octahedral configuration –a); the comparison of emission spectra of Fe^{3+} doped spinels recorded at -150°C –b); the maximal emission energy as a function of CFS –c); the decay profiles of Fe^{3+} luminescence –d).

In order to verify the optical response of Fe^{3+} doped spinels to temperature changes their emission spectra were measured in a wide temperature range (-150ºC – 300ºC). The intensity of the emission band for all of investigated materials decreases at elevated temperatures which is related to thermally activated nonradiative depopulation channel of the excited states (Fig. 4 a-d). At elevated temperatures, when the provided thermal energy exceeds the so-called activation energy ΔE, the nonradiative processes dominate over the radiative ones. The value of ΔE, which express the energy of the intersection point between the ground and excited state parabolas, can be directly determined based on the emission intensity measurement vs temperature according to the methodology presented in the SI (eq. S1). In the case of the analyzed phosphors, ΔE decreases as follows:1234.03 cm^{-1}, 1225.96 cm^{-1}, 879.14 cm^{-1} and 871.08 cm^{-1} for MAO, MGO, CAO and CGO, respectively. Therefore, the emission intensity of Fe^{3+} ions in the MAO and MGO decreases gradually with temperature and even at 300ºC some evidence of Fe^{3+} luminescence remains. On the other hand, in the case of CAO and CGO the intensity drastically drops down by over two orders of magnitude in the analyzed temperature range. This effect is directly reflected in the case of the $T_{1/2}$ parameter which represents the temperature at which emission intensity decreases to its half value (Fig. 4f). When the host material composition changes the $T_{1/2}$ increases from -90ºC for CGO to 150ºC for MAO. This observation enables the modification of the thermal stability of luminescence intensity Fe^{3+} doped phosphor based on the chemical composition of the host material. It is worth mentioning that the usable temperature range (UTR) in which a given phosphor can be applied for noncontact temperature sensing is also dependent on the host material composition. The UTR in the cases of CAO and MAO is limited to the -150 – 150 ºC range, while CGO and MGO can be applied in the whole analyzed temperature range (Fig. 4 e). The strong of susceptibility emission intensity of Fe^{3+} doped spinels to temperature changes indicates their potential to noncontact temperature sensing. Therefore, to quantify these properties the relative thermal sensitivity (S_R) of the luminescent thermometer was calculated as follows:

$$S_R = \frac{1}{A}\frac{\Delta A}{\Delta T}\cdot 100\% \qquad (1)$$

where A corresponds to the temperature-dependent parameter and ΔA represents the change of A for ΔT temperature variations. In the case of S_{R1} the parameter A represents the emission intensity of the Fe^{3+} ions and the results of performed calculation of S_{R1} as a function of temperature are depicted in Fig. 4 g. According to the expectation, the host material composition has a high impact on the relative sensitivity values of Fe^{3+}- based luminescent thermometer. The highest S_{R1} values were found for CAO and CGO nanocrystals as a consequence of the most dynamic changes of Fe^{3+} emission intensity in the -150°C – 150°C temperature range. Therefore obtained S_{R1max} were 1.73%/°C (at 0°C) and 2.12%/°C (at 6°C) for CAO and CGO, respectively (Fig. 4 e, g). It is worth noting that in the case of CAO:Fe^{3+} and CGO:Fe^{3+} the usable temperature range in which temperature readout with S_R>1%/°C is very wide. In turn, the MAO and MGO compounds reveal similar S_{R1} distribution and definitely lower S_{R1} which rises with the temperature enhancement, reaching the maximum of 0.71%/°C and 1.0%/°C, respectively (Fig. 4 g). A strong correlation between the host material composition and S_{R1} is observed for the temperature of 0°C, namely which increases in the following order: 0.2%/°C (MAO), 0.32%/°C (MGO), 1.73%/°C (CAO) and 2.07%/°C (CGO) (Fig. 4 h). It is worth emphasizing, that much higher Sr values are obtained for Fe^{3+} ions localized in the crystallographic sites of lower symmetry. (Fig. 4 g).

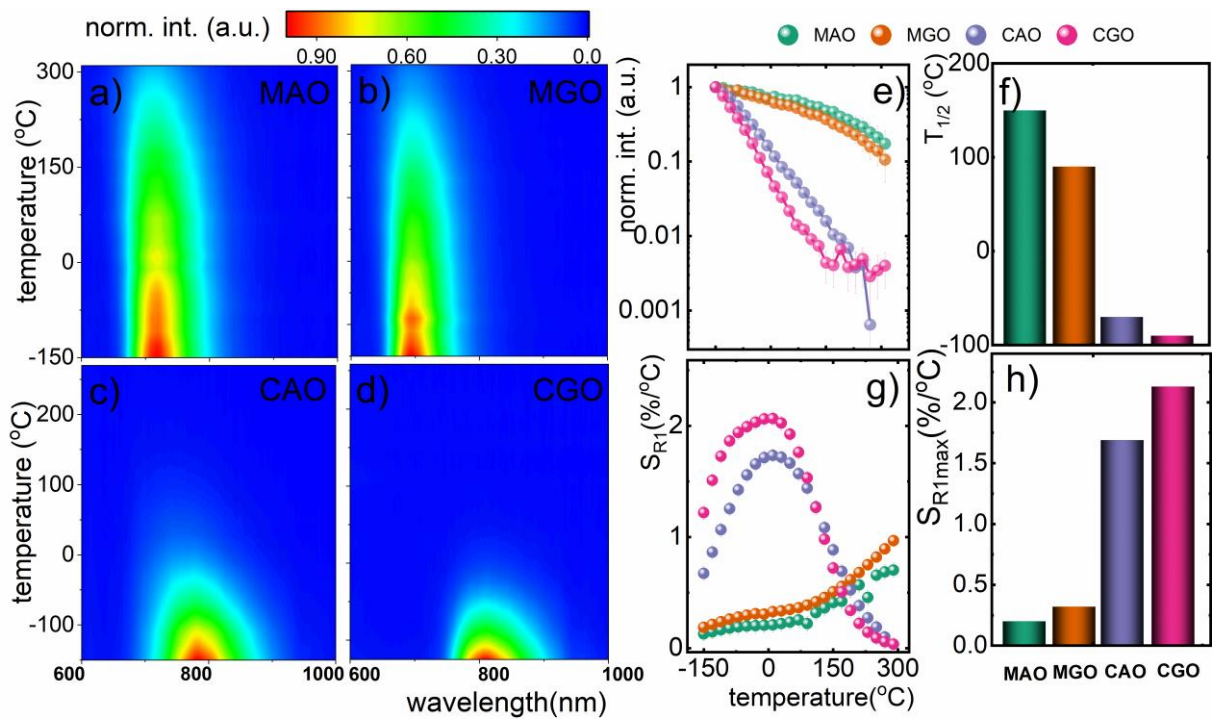

Fig. 4. The emission maps at different temperatures for MAO, MGO, CAO and CGO – a), b), c), d), respectively; the Fe^{3+} emission intensity as a function of temperature – e), the temperature at which the emission intensity is at half is initial value – f); the relative sensitivities of Fe^{3+}- based spinel luminescence thermometers at 0ºC –g); the comparison of the relative sensitivity values for different host material composition–h).

Although the emission intensity of the band associated with $^4T_1$ (^4G)→$^6A_1$ (^6S) electronic transition reveals high susceptibility to thermal quenching, the intensity-based luminescent thermometers are considered as temperature sensors of relatively low reliability because emission intensity may be affected by many experimental parameters leading to the erroneous temperature readout. Therefore to enhance the reliability of temperature readout a ratiometric luminescent thermometer has been developed by the co-doping of Fe^{3+} doped spinels with lanthanide ion (Ln^{3+}). This was motivated by the fact that the spectroscopic properties of lanthanide ions are considered to be less thermally dependent with respect to the TM ions[11,13,16]. It should be noted . In this particular case, the Tb^{3+} ions were used as a internal reference because their emission bands occur in the spectral range which does not overlap with the Fe^{3+} band and due to the relatively large energy gap between the emitting $^5D_4$ state of Tb^{3+} and the next lower laying $^7F_0$ one, largely minimizing the probability of its luminescence thermal quenching.

To verify and confirm the potential of Fe^{3+}, Tb^{3+} - co-doped $MgAl_2O_4$, $MgGa_2O_4$, $CaAl_2O_4$, $CaGa_2O_4$ nanocrystals to temperature sensing, the emission spectra were measured in the range of -150ºC – 300ºC under 266 nm of irradiation (Fig. 5 a-d). It has been shown that the UV excitation provides the simultaneous emission of both Tb^{3+} and Fe^{3+} ions. The emission spectra of Tb^{3+} ions embedded in the spinel host materials consist of four narrow bands with the maximum at 490 nm, 543 nm, 588 nm and 625 nm, being assigned to $^5D_4$→ $^7F_6$, $^5D_4$→ $^7F_5$, $^5D_4$→ $^7F_4$ and $^5D_4$→ $^7F_3$ electronic transitions of Tb^{3+} ions, respectively (Fig. 5 e). Besides, in the case of $CaAl_2O_4$ nanocrystal two additional Tb^{3+} peaks are observed, related to the luminescence coming from the higher energy level, i. e. $^5D_3$→ $^7F_5$ (λ_{em} = 417 nm) and $^5D_3$→ $^7F_4$ (λ_{em} = 436 nm) (Fig. 5 e). The population of the Tb^{3+} emitting levels takes place via UV activated spin-allowed $4f^8(^7F_6)$→$4f^75d^1$ electronic transition which is followed by the nonradiative depopulation to the $^5D_3$ excited state and sequentially to the $^5D_4$ one (Fig. 5 e). It is evident, that for all host materials the luminescence thermal quenching of Fe^{3+} occurs, whereas the Tb^{3+} luminescence in the MAO, CAO and CGO lattices is

to a lesser extent susceptible to the temperature changes in respect to the Fe^{3+} emission (Fig. 5 a, b, d). It needs to be noting here that, the Tb^{3+} emission undergoes the thermal quenching in the MGO material (Fig. 5 c). This is because the f-d absorption band of Tb^{3+} ions, in this case, is of very low intensity and the dominant process of the Tb^{3+} emission generation upon λ_{exc}=266 nm is the $Fe^{3+}\rightarrow Tb^{3+}$ energy transfer (Fig. 5 e). The confirmation of the opposite $Tb^{3+}\rightarrow Fe^{3+}$ energy transfer was given by the measurement of the excitation spectra as a function of temperature. The representative thermal evolution of excitation spectra measured for Fe^{3+} luminescence for CGO:Fe^{3+},Tb^{3+} nanocrystals is shown in Fig. S4. The enhancement of the temperature leads to the occurrence of the additional bands localized at around 375 nm and 475 nm associated with the $^7F_6\rightarrow{}^5L_{10}$ and $^7F_6\rightarrow{}^5D_4$ electronic transitions of the Tb^{3+} ions, respectively. Therefore the lowering of the population of the excited state of Fe^{3+} reduces the population of the $^5D_4$ emitting state of Tb^{3+} ion. However, its emission is still not totally quenched even at 300°C[51]. On the other hand in the case of MAO, CAO and CGO slight enhancement of Tb^{3+} emission intensity with an increase of temperature can be observed. This is associated with the thermally activated $Fe^{3+}\rightarrow Tb^{3+}$ energy transfer which leads to the enhancement of Fe^{3+} luminescence thermal quenching. The opposite thermal monotonicity of Fe^{3+} and Tb^{3+} emission signals should facilitate the thermometric performance of Fe^{3+}, Tb^{3+}-based ratiometric luminescent thermometer. Therefore to evaluate the ability of Fe^{3+}, Tb^{3+}- doped spinel to noncontact temperature sensing, the luminescence intensity ratio (LIR) parameter was calculated as follows:

$$LIR = \frac{Fe^{3+}(^4T_1 \rightarrow {}^2T_2)}{Tb^{3+}(^5D_4 \rightarrow {}^7F_5)} \qquad (2)$$

It is clearly seen that in the case of MAO the LIR parameter reveals very similar thermal dependence to the Fe^{3+} emission intensity itself presented in Fig. 4 e (see also Fig. S5), which results from the thermal quenching of the Fe^{3+} emission and almost temperature-independent emission intensity of Tb^{3+} ions (Fig. 5 f). The enhancement of the Tb^{3+} emission intensity in MGO mentioned before causes an increase of LIR with a temperature above -100°C. However, for the host materials of low CFS (CAO, CGO) the LIR is quenched definitely faster with respect to the corresponding Fe^{3+} emission intensities themselves, what

results from the thermally induced $Fe^{3+}\rightarrow Tb^{3+}$ energy transfer (Fig. 5 e, f). As a consequence, any evidence of the $^4T_1$ (^4G)$\rightarrow$$^6A_1$ (^6S) emission band cannot be observed in CAO:Fe^{3+},Tb^{3+} and CGO: Fe^{3+},Tb^{3+} above 100°C. In order to quantify the thermal dependence of LIR, the relative sensitivity S_{R2} was calculated according to eq. 2 (where A is LIR in this case). The maximal values of S_{R2} were found to be 2.58%/°C at 10°C and 2.08%/°C at -10°C for CAO and CGO, respectively (Fig. 5g). This effect confirms that the presence of Tb^{3+} codopant not only improvesthe reliability of temperature readout but also enhances the relative sensitivity of thermometer to temperature changes. Bearing in mind the potential implementation of investigated materials into temperature sensing, the temperature measurement uncertainty (δT) of developed ratiometric luminescence nanothermometers must be considered (eq. S2). Of all thoroughly analyzed Fe^{3+}, Tb^{3+} -co-doped spinels, the smallest value of δT possesses the CAO:Fe^{3+},Tb^{3+} one, where the δT_{max} was found to be 0.35°C (Fig. S6). Moreover this material is characterized by the lowest δT value in the range of biological temperatures, namely 0.26°C. Taking advantage of the high sensitivity value (S_{Rmax}= 2.58%/°C), falling at physiological temperatures as well as the low temperature measurement uncertainty, the CAO:Fe^{3+},Tb^{3+} - based luminescence thermometer reveals excellent performance to temperature monitoring. Investigated luminescent thermometers reveal very high repeatability of the noncontact temperature readout what was confirmed during several heating cooling cycles (Fig. 5 h and i, see also Fig. S7).

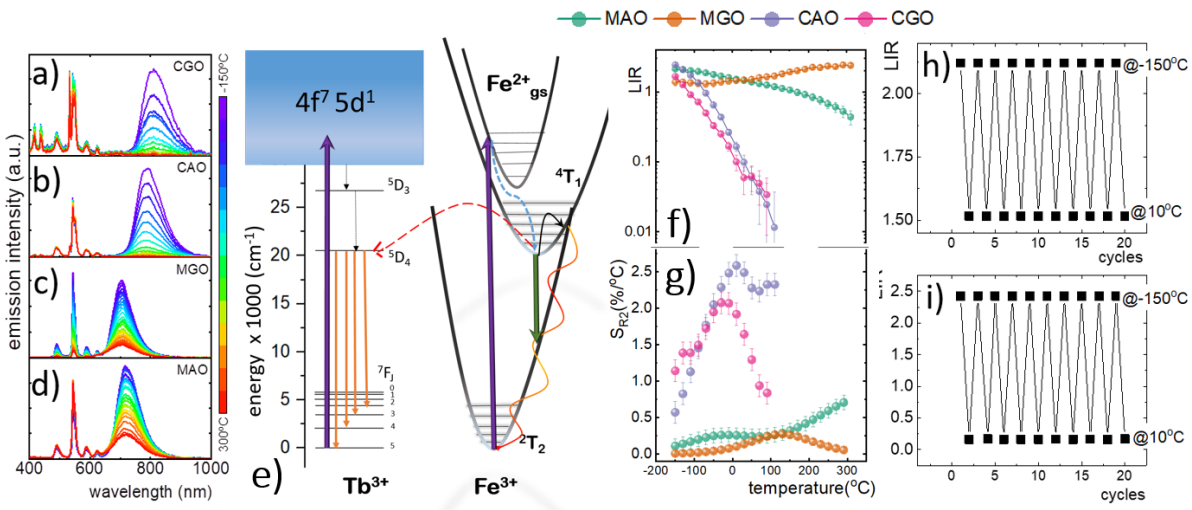

Figure 5. Thermal evolution of emission spectra of MAO-a), MGO-b), CAO-c) and CGO –d) nanocrystals co-doped with Fe^{3+}, Tb^{3+} ions; schematic simplified energy diagrams of Tb^{3+} and Fe^{3+} ions with specified $Fe^{3+}\rightarrow Tb^{3+}$ (red dashed line) –e); thermal dependence of LIR parameters –f); and corresponding relative sensitivities–g); LIR values during several heating-cooling cycles for MAO-h) and CAO-i).

The comparison of the thermometric properties of Fe^{3+}- based luminescence nanothermometers is presented in Table 2. Among all the Fe^{3+}-based noncontact temperature sensors the highest relative sensitivity values were found for garnet type materials. However, it needs to be noticed that in that case the high S_R was obtained by the introduction of additional transition metal ion (Cr^{3+}) co-dopant in order to activate additional channel of nonradiative depopulation of Fe^{3+} excited state via $Fe^{3+}\rightarrow Cr^{3+}$ energy transfer. Therefore values of S_R for Fe^{3+} doped spinels presented in this manuscript are one of the highest reported for Fe^{3+} based luminescent thermometers up to date. As it was shown presented both spectral ranges of the optical response and the thermometric performance including relative sensitivity and usable temperature range can be easily modulated by the crystal field strength, in particular the metal-to-oxygen distance. This approach not only enables to optimize the properties of the luminescent thermometer by the modification of the host material composition but first of all it allows for the prediction of the thermometric properties of luminescent thermometer based on its crystallographic data and thus intentional development of the highly sensitive luminescent thermometer. It needs to be noted here that the emission intensity is one of the most important parameters of the luminescent thermometer which affects the signal-to-noise ratio and hence the uncertainty of thermal sensing and imaging and this parameter should also be considered. In the case of the materials under investigation in this manuscript, the strongest emission intensity was found for MAO while the lowest for CAO. Nevertheless, the reasonable values of calculated thermal uncertainties confirm the high applicative potential of presented luminescent thermometers. The obtained high values of S_R makes the Fe^{3+} interesting alternative for well-established lanthanide-based luminescent thermometers. One of the most important advantages of Fe^{3+}-based temperature sensors in the easiness in the modulation of their optical properties by the crystal field strength or the local ions symmetry modification that is not feasible in the case of Ln^{3+}. However, it should be noticed that the main disadvantage of the material

described in this manuscript for noncontact temperature sensing in the UV excitation line required to generate Fe^{3+} luminescence that significantly limits the potential application fields .

Table 2. Comparison of the thermometric performance of different Fe^{3+} based luminescent thermometers.

Luminescence thermometer	λ_{exc} (nm)	max λ_{exc} (nm)	S_{Rmax} (%/°C)	T $_{SRmax}$ (°C)	UTR (°C)	Ref.
$LiAl_5O_8:Fe^{3+}$	266	660	0.95	-100	-150 – 300	38
$LiAl_5O_8:Fe^{3+}, Nd^{3+}$	266, 808 separately	660	0.56	-80	-150 – 50	38
$LiAl_5O_8:Fe^{3+}$	266	665	~1.68	~572	326.85 – 926.85	52
$YAG:Fe^{3+}, Cr^{3+}$	266	780	4.80	200	-150 – 300	29
$YGG:Fe^{3+}, Cr^{3+}$	266	805	3.30	50	50 – 200	29
$GGG:Fe^{3+}, Cr^{3+}$	266	786	2.30	45	-30 – 200	29
$LuGG:Fe^{3+}, Cr^{3+}$	266	825	2.62	0	-50 – 200	29
$YAG:Fe^{3+}, Cr^{3+}, Nd^{3+}$	266	780	0.96	150	50 – 150	29
$YGG:Fe^{3+}, Cr^{3+}, Nd^{3+}$	266	805	1.68	50	-150 – 150	29
$GGG:Fe^{3+}, Cr^{3+}, Nd^{3+}$	266	786	1.57	50	-150 – 150	29
$LuGG:Fe^{3+}, Cr^{3+}, Nd^{3+}$	266	825	5.90	100	-150 – 150	29
$MgAl_2O_4:Fe^{3+}$	266	719	0.71	290	-150 – 310	This work
$MgGa_2O_4:Fe^{3+}$	266	696	1.0	290	-150 – 310	This work
$CaAl_2O_4:Fe^{3+}$	266	782	1.73	0	-150 – 150	This work
$CaGa_2O_4:Fe^{3+}$	266	809	2.12	6	-150 – 150	This work
$MgAl_2O_4:Fe^{3+}, Tb^{3+}$	266	719	0.74	300	-150 – 310	This work
$MgGa_2O_4:Fe^{3+}, Tb^{3+}$	266	696	0.27	130	-150 – 210	This work
$CaAl_2O_4:Fe^{3+}, Tb^{3+}$	266	782	2.58	10	-150 – 110	This work
$CaGa_2O_4:Fe^{3+}, Tb^{3+}$	266	809	2.08	-10	-150 – 30	This work

Conclusions

In this work, an approach to modulate the spectral position and the luminescence thermal quenching rate of Fe^{3+} ions by modifying the change of the crystal field strength (CFS) and the local ions symmetry induced by the host material composition in the AB_2O_4 type nanocrystals (A= Mg, Ca; B=Al, Ga) was presented. In order to validate the proposed approach, the spectroscopic properties of $MgAl_2O_4$, $MgGa_2O_4$, $CaAl_2O_4$, $CaGa_2O_4$ nanocrystals doped with Fe^{3+} ions were investigated. It was shown that by the change of the composition of the phosphor the effective metal to oxygen distance in cationic site substituted by the Fe^{3+} ions can be enlarged causing the reduction of the crystal field strength. Moreover, the change of the host material composition and thus reduction of the local point symmetry of Fe^{3+} ion leads to the broadening and the redshift of its emission band and shorthening of the excited state lifetime. The host material composition modifies also the thermal stability of Fe^{3+} luminescence. The evident increase of the $T_{1/2}$ parameter from -90°C for CGO to 180°C for MAO as a the local point symmetry increases from C_1 to O_h indicates that the thermal stability of Fe^{3+} doped spinels can be intentionally designed by the deliberate selection of the host material composition. Therefore the host materials of the cationic sites of low point symmetries substituted by Fe^{3+} are especially favorable from the thermometric perspective. The exceptional susceptibility of Fe^{3+} emission intensity to temperature quenching enables the development of a highly sensitive luminescent thermometer. In the case of the Fe^{3+} intensity-based luminescent thermometer, its

relative sensitivity at 0ºC decreases from 2.07%/ºC for CGO to 0.2%/ºC for MAO. In order to enhance the reliability of temperature readout, the ratiometric approach was used by the introduction of the Tb^{3+} co-dopant ions as a internal reference signal. In the case of the ratiometric approach, an increase of S_R to 2.58%/ºC for CAO was found. The proposed approach clearly confirms that the spectroscopic properties of the Fe^{3+} based luminescent thermometers including the spectral range of the emission band and the lifetime of the Fe^{3+} excited state as well as the thermometric properties of luminescent thermometer involving the relative sensitivity and the usable temperature range may be controlled by the intensional design of the host material composition.

Conflicts of interest

There are no conflicts to declare.

Acknowledgements

The authors would like to acknowledge the reviewers of the manuscript for their substantial contribution to the interpretation of the described results. The ‘‘High sensitive thermal imaging for biomedical and microelectronic application’’ project is carried out within the First Team programme of the Foundation for Polish Science co-financed by the European Union under the European Regional Development Fund. The financial support from the European Union’s Horizon 2020 FET Open program under grant agreement no. 801305 is acknowledged. LDC thanks the project CICECO-Aveiro Institute of Materials, UIDB/50011/2020 & UIDP/50011/2020, financed by Portuguese funds through the FCT/MEC and when appropriate co-financed by FEDER under the PT2020 Partnership Agreement.

References

1 A. Luchechko, Y. Zhydachevskyy, S. Ubizskii, O. Kravets, A. I. Popov, U. Rogulis, E. Elsts, E. Bulur and A. Suchocki, *Sci. Rep.*, 2019, **9**, 9544.
2 R. Cao, F. Zhang, C. Cao, X. Yu, A. Liang, S. Guo and H. Xue, *Opt. Mater. (Amst).*, 2014, **38**, 53–56.
3 M. G. Brik, J. Papan, D. J. Jovanović and M. D. Dramićanin, *J. Lumin.*, 2016, **177**, 145–151.
4 V. Singh, R. P. S. Chakradhar, J. L. Rao and J.-J. Zhu, *Mater. Chem. Phys.*, 2008, **111**, 143–148.
5 M. Rai, K. Mishra, S. B. Rai and M. P., *Mater. Res. Bull.*, 2018, **105**, 192–201.
6 M. Rai, S. K. Singh and P. Morthekai, *Opt. Lett.*, 2016, **41**, 3635.
7 Y. Wu, Y. Zhuang, R.-J. Xie, K. Ruan and X. Ouyang, *Dalt. Trans.*, 2020, **49**, 3606–3614.
8 E. H. Song, Y. Y. Zhou, Y. Wei, X. X. Han, Z. R. Tao, R. L. Qiu, Z. G. Xia and Q. Y. Zhang, *J. Mater. Chem. C*, 2019, **7**, 8192–8198.
9 A. Abdukayum, J.-T. Chen, Q. Zhao and X.-P. Yan, *J. Am. Chem. Soc.*, 2013, **135**, 14125–14133.
10 A. Bednarkiewicz, L. Marciniak, L. D. Carlos and D. Jaque, *Nanoscale*, 2020, **12**, 14405–14421.
11 M. Suta and A. Meijerink, *Adv. Theory Simulations*, 2020, **n/a**, 2000176.
12 L. Marciniak, A. Bednarkiewicz, D. Kowalska and W. Strek, *J. Mater. Chem. C*, 2016, **4**, 5559–5563.
13 C. D. S. Brites, P. P. Lima, N. J. O. Silva, A. Millán, V. S. Amaral, F. Palacio and L. D. Carlos, *Nanoscale*, 2012, **4**, 4799.

14 F. Vetrone, R. Naccache, A. Zamarrón, A. Juarranz de la Fuente, F. Sanz-Rodríguez, L. Martinez Maestro, E. Martín Rodriguez, D. Jaque, J. García Solé and J. A. Capobianco, *ACS Nano*, 2010, **4**, 3254–3258.
15 D. Jaque and F. Vetrone, *Nanoscale*, 2012, **4**, 4301.
16 C. D. S. Brites, S. Balabhadra and L. D. Carlos, *Adv. Opt. Mater.*, 2019, **7**, 1801239.
17 B. Jiang, F. Chi, X. Wei, Y. Chen and M. Yin, *J. Appl. Phys.*, , DOI:10.1063/1.5024771.
18 N. Basavaraju, S. Sharma, A. Bessière, B. Viana, D. Gourier and K. R. Priolkar, *J. Phys. D. Appl. Phys.*, 2013, **46**, 375401.
19 S. K. Sharma, D. Gourier, B. Viana, T. Maldiney, E. Teston, D. Scherman and C. Richard, in *Optical Materials*, 2014.
20 Y. Zhuang, J. Ueda and S. Tanabe, *J. Mater. Chem. C*, 2013, **1**, 7849.
21 B. Viana, S. K. Sharma, D. Gourier, T. Maldiney, E. Teston, D. Scherman and C. Richard, *J. Lumin.*, 2016, **170**, 879–887.
22 J. Wang, Q. Ma, X. Hu, H. Liu, W. Zheng, X. Chen, Q. Yuan and W. Tan, *ACS Nano*, 2017, **11**, 8010–8017.
23 T. Maldiney, A. Bessière, J. Seguin, E. Teston, S. K. Sharma, B. Viana, A. J. J. Bos, P. Dorenbos, M. Bessodes, D. Gourier, D. Scherman and C. Richard, *Nat. Mater.*, 2014, **13**, 418–426.
24 A. Kobylinska, K. Kniec, K. Maciejewska and L. Marciniak, *New J. Chem.*, 2019, **43**, 6080–6086.
25 J. Ueda, M. Back, M. G. Brik, Y. Zhuang, M. Grinberg and S. Tanabe, *Opt. Mater. (Amst).*, 2018, **85**, 510–516.
26 E. Glais, M. Pellerin, V. Castaing, D. Alloyeau, N. Touati, B. Viana and C. Chanéac, *RSC Adv.*, 2018, **8**, 41767–41774.
27 J. Yang, Y. Liu, Y. Zhao, Z. Gong, M. Zhang, D. Yan, H. Zhu, C. Liu, C. Xu and H. Zhang, *Chem. Mater.*, 2017, **29**, 8119–8131.
28 D. Chen, Z. Wan, Y. Zhou and Z. Ji, *J. Eur. Ceram. Soc.*, 2015, **35**, 4211–4216.
29 K. Kniec, K. Ledwa, K. Maciejewska and L. Marciniak, *Mater. Chem. Front.*, 2020, **4**, 1697–1705.
30 K. Kniec and L. Marciniak, *Sensors Actuators B Chem.*, 2018, **264**, 382–390.
31 K. Trejgis and L. Marciniak, *Phys. Chem. Chem. Phys.*, 2018, **20**, 9574–9581.
32 L. Marciniak, A. Bednarkiewicz and W. Strek, *Sensors Actuators, B Chem.*, 2017, **238**, 381–386.
33 Kniec, Ledwa and Marciniak, *Nanomaterials*, 2019, **9**, 1375.
34 K. Elzbieciak, A. Bednarkiewicz and L. Marciniak, *Sensors Actuators B Chem.*, 2018, **269**, 96–102.
35 L. Marciniak and K. Trejgis, *J. Mater. Chem. C*, 2018, **6**, 7092–7100.
36 C. Matuszewska and L. Marciniak, *J. Lumin.*, 2020, **223**, 117221.
37 M. G. Brik, J. Papan, D. J. Jovanović and M. D. Dramićanin, *J. Lumin.*, 2016, **177**, 145–151.
38 K. Kniec, M. Tikhomirov, B. Pozniak, K. Ledwa and L. Marciniak, *Nanomaterials*, 2020, **10**, 189.
39 C. D. S. Brites, P. P. Lima, N. J. O. Silva, A. Millán, V. S. Amaral, F. Palacio and L. D. Carlos, *Adv. Mater.*, 2010, **22**, 4499–4504.
40 R. Piñol, C. D. S. Brites, R. Bustamante, A. Martínez, N. J. O. Silva, J. L. Murillo, R. Cases, J. Carrey, C. Estepa, C. Sosa, F. Palacio, L. D. Carlos and A. Millán, *ACS Nano*, 2015, **9**, 3134–3142.
41 J. L. Wang, E. H. Song, M. Wu, W. B. Dai, S. Ye and Q. Y. Zhang, *Mater. Res. Bull.*, 2016, **74**, 340–345.
42 H. . Hoerkner, W., Moller-Buschbaum, *J. Inorg. Nucl. Chem.*, 1976, 983–984.
43 K. A. Gedekar, S. P. Wankhede, S. V. Moharil and R. M. Belekar, *J. Adv. Ceram.*, 2017, **6**, 341–350.
44 R. Cao, F. Zhang, C. Cao, X. Yu, A. Liang, S. Guo and H. Xue, *Opt. Mater. (Amst).*, 2014, **38**, 53–56.
45 H. J. Deiseroth and H. M►ller -Buschbaum, *Zeitschrift f►r Anorg. und Allg. Chemie*, 1973, **396**, 157–164.
46 H. J. Deiseroth and H.-K. M►ller-Buschbaum, *Zeitschrift f►r Anorg. und Allg. Chemie*, 1973, **402**, 201–205.
47 R. J. Wiglusz and T. Grzyb, *Opt. Mater. (Amst).*, 2011, **33**, 1506–1513.
48 H. Liu, L. Yu and F. Li, *J. Phys. Chem. Solids*, 2013, **74**, 196–199.
49 N. Kumar, B. Marí, J. Jindal, A. Mittal, K. Kumari and S. Maken, *Mater. Today Proc.*, 2019, **19**, 646–649.
50 L. Alyabyeva, V. Burkov and B. Mill, *Opt. Mater. (Amst).*, 2015, **43**, 55–58.
51 J. Drabik, K. Ledwa and L. Marciniak, *Nanomaterials*, 2020, **10**, 1333.
52 J. Brübach, T. Kissel, M. Frotscher, M. Euler, B. Albert and A. Dreizler, *J. Lumin.*, 2011, **131**, 559–564.